applied sciences

MDPI

Article

Distribution and Prediction of Incremental Cutter Flank Wear in High-Efficiency Milling

Peiyi Zhao, Yufeng Song, Bin Jiang * and Bin Wang

Key Laboratory of Advanced Manufacturing and Intelligent Technology, Ministry of Education, Harbin University of Science and Technology, Harbin 150080, China; zhaopeiyi@hrbust.edu.cn (P.Z.)
* Correspondence: hrbust1216@163.com

Abstract: In the milling of titanium alloy workpieces, tool wear seriously affects the surface quality of a workpiece and its tool life. It is of great significance to study the influence of instantaneous contact stiffness on instantaneous friction variables and incremental wear, which is of great significance for the realization of control over the degree of flank wear and improving the service life of cutter teeth. In this paper, an experiment to monitor cutting with a Ti6Al4V workpiece with a high-feed milling cutter was carried out; according to the experimental results, the wear area of the flank face of the cutter tooth was determined. The feature points of the flank were selected, and an instantaneous contact stiffness calculation method for the flank was proposed. The infinitesimal method was used to characterize the distribution of the contact stiffness of the flank, and the evolution characteristics of instantaneous contact stiffness distribution under the influence of vibration were obtained. According to the calculation results, the instantaneous distribution of flank wear depth was calculated. A grey correlation degree was used to reveal the correlation between the instantaneous contact stiffness of the flank face and wear depth, and a positionable wear-prediction model based on the instantaneous contact stiffness of the flank was proposed. Based on a BPNN (back propagation neural network), a prediction model for flank wear was established. The results showed that the above model and method could accurately predict the instantaneous wear of the tool flank.

Keywords: milling cutter; cutter tooth flank; instantaneous contact stiffness; wear distribution; wear prediction

check for updates

Citation: Zhao, P.; Song, Y.; Jiang, B.; Wang, B. Distribution and Prediction of Incremental Cutter Flank Wear in High-Efficiency Milling. *Appl. Sci.* **2023**, *13*, 4749. https://doi.org/10.3390/app13084749

Academic Editor: Arkadiusz Gola

Received: 10 March 2023
Revised: 27 March 2023
Accepted: 6 April 2023
Published: 10 April 2023

Copyright: © 2023 by the authors. Licensee MDPI, Basel, Switzerland. This article is an open access article distributed under the terms and conditions of the Creative Commons Attribution (CC BY) license (https://creativecommons.org/licenses/by/4.0/).

1. Introduction

The friction generated by a high-efficiency milling cutter in the cutting process directly affects the tool's wear. This phenomenon is inevitable in the machining process and is affected by many factors [1,2]. With improvements to the technical requirements made, more complex and difficult-to-machine composite materials are used in the aviation industry, which have good heat resistance and oxidation resistance. In its machining process, workpiece loss is fast, with a short service life [3,4]. The wear of milling cutter teeth will affect the service life of milling cutters and limit the further development and application of high-efficiency cutting technology. Therefore, it is necessary to conduct in-depth research on the friction behavior of high-efficiency milling cutters and the prediction of tool tooth wear.

At present, the main bottleneck in the field of machining is tool wear and the resulting shortening of tool life, which ultimately leads to low machining accuracy and low productivity [5]. Tool life is basically defined as the time required to reach a predetermined flank wear width, and tool condition and life prediction are the most relevant factors in identifying the state of tool wear [6,7]. The judgment of tool wear and breakage in existing industrial applications is mainly based on experience through passive shutdown and manual inspection [8]. If the tool is replaced too early, it will directly reduce processing efficiency and increase manufacturing costs. In recent years, in order to give full play to the

maximum cutting performance of a tool, an important development trend has been the use of on line real-time monitoring technology to study tool wear and damage, which is very important for the realization of CNC machining, with few people (or even none) attending the tool, or with one person attending multiple machines [9].

There are three important time stages in the evolution of typical tool wear failure within the cutting process: the initial stage of wear, the stable wear stage, and the accelerated damage stage [10]. In the early 20th century, American engineer Taylor developed a model to monitor tool wear and found that the factors affecting tool wear are cutting speed > feed > cutting depth [11].

In addition, domestic and foreign scholars have carried out a lot of research on other factors that cause tool wear. Sick [12] studied tool wear from the perspective of direct and indirect methods and analyzed and summarized the problem of tool wear monitoring in the cutting process in detail. A total of 87% of the literature proposes a multisensor method for monitoring typical process parameters, such as tool force, vibration, and acoustic emission signals. Ni et al. [13] carried out external ultrasonic vibration excitation on a workpiece and evaluated surface morphology quality under different tool wear conditions from the perspective of workpiece dynamics and kinematics. Mao et al. [14] studied the effect of different tool coating materials on tool tooth wear through a large number of cutting experiments. Bouzakis et al. [15] showed that the cutting load caused by the super-stress state during the cutting process affected the early failure of the coating and further showed that cutting could cause tool friction and wear. Rehorn et al. [16] analyzed and summarized the problem of tool condition monitoring from the perspective of different processing methods. Cai et al. [17] considered five parameters: workpiece size, radius, cutting allowance, cutting depth, and cutting angle to study the influence of the contact area of cutter and workpiece on tool wear and concluded that the cutting depth and cutting angle have the greatest influence on tool wear. Oliveira and Diniz [18] studied the influence of different workpiece inclination angles on tool wear. The results show that the degree of tool wear increases with the increase in surface inclination angle, and, in the early cutting process, tool wear occurs mainly due to the diffusion wear of the flank; in the later cutting process, tool wear is mainly caused by adhesive wear and microchipping. The above research is based on a large number of experiments, but the identification results are greatly affected by uncertain interference without the support of cutting force model and wear model.

The wear of the cutter tooth causes a change in the geometric structure of the cutting edge and the flank, which changes the instantaneous contact stiffness and its distribution within the flank, resulting in the uneven distribution of friction and wear degree over the flank, making the evolution of the friction and wear of the milling cutter difficult to predict, with the service life of the cutter decreasing.

In a study of the stiffness of the machining system in the cutting process, Liao et al. [19] proposed a method to identify the contact behavior of the cutter handle joint surface and concluded that the contact stiffness and total contact force decreased significantly at high speed. Feng et al. [20] established a unified damping model for milling systems with different stiffnesses, revealing the relationship between stiffness changes and shear force coefficients. Lorenzo et al. [21] proposed a dynamic stiffness model to consider the static and dynamic effects, revealing the influential factors of forced tool vibration on the cutting parameters and stiffness. Nguyen et al. [22] simulated the influence of cutting force on the stiffness deflection of a tool spindle and proposed a data-monitoring method for the state of a machine tool, studying the initial inclination angle of the tool and the stiffness of the spindle system. Liu et al. [23] considered the change in instantaneous cutting force, the change in contact stiffness between the workpiece and the additional tool support, and the change in workpiece thickness during the milling process and proposed a prediction model for the influence of additional tooltip support on the machining surface error in the peripheral milling of flexible workpieces. Schmitz et al. [24] proposed a finite element modeling method to determine the stiffness and damping behavior between a tool and the

fixture in the heat shrink-fit connection. Liu et al. [25] proposed a design method for the interface between the spindle and the tool holder by using fractal theory and a multiscale contact mechanic model. The effects of cutting force, average roughness, material type, and other factors were analyzed. The effects of performance, preload, and temperature change on contact stiffness were discussed.

For a long time, many scholars have been concerned about the real-time monitoring of tool wear and breakage during machining. At present, it can be divided into direct monitoring and indirect monitoring. The direct monitoring method is used to quantify tool wear and damage status through image vision and infrared measurement [26]. However, these methods need to interrupt the processing process and affect processing efficiency; at the same time, the direct monitoring method is expensive and limited by the operating environment due to the continuous contact between the tool and the workpiece, as well as the harsh processing environment (cutting fluid and chips). The application of the direct monitoring method in the actual machining process has great limitations [27]. The indirect monitoring method is used to identify the state of tool wear in real time via generated data by analyzing the signal received by the sensor generated by the milling cutter during the machining process. The indirect method measures tool wear by extracting cutting force, vibration rate, and current [28]. The main advantage of these methods is that the monitoring process does not need to stop, making up for the lack of direct monitoring methods. Among these methods, although a pure data method based on artificial intelligence has achieved good monitoring results with its strong nonlinear fitting ability [29], the method based on a physical model can analyze the relationship between wear damage variables and monitoring targets by using a clear causal mechanism, which has also been widely recognized and studied by scholars.

In the existing research, the machining process, cutter tooth trajectory, and milling cutter cutting parameters are mostly constant values. The complex cutter tooth flank, cutting parameters, and cutter tooth trajectory may change during the machining process. The existing monitoring and prediction models cannot meet the actual machining. Most of the existing prediction methods are used for the prediction of overall tool life, which cannot achieve life prediction of a specific point. Therefore, it is necessary to design a tool flank wear model that can be positioned and predicted without solving the above problems. Most of the existing tool wear prediction models are mainly based on the acquisition of external forces, such as cutting force and positive pressure, as data collection [30]. However, there are few prediction models that consider the internal forces and external forces of the tool at the same time. The contact stiffness is affected by positive pressure and deformation. According to the above ideas, it is necessary to propose a positionable, tool-flank wear prediction model based on the instantaneous contact stiffness of the tool flank.

2. Milling Cutter Tooth Flank Feature Point-Selection Method

In order to reveal the distribution of contact stiffness and incremental wear between the cutter tooth and the machined transition surface of the workpiece during the cutting process, the experiment of cutting titanium alloy (Ti6Al4V) with a high-feed cemented carbide milling cutter was carried out, and is reported in this paper.

The experimental scheme is shown in Table 1, and a picture of the cutting experiment scene is shown in Figure 1a. The machine model was VDL-1000E (three-axis milling machining center), and the milling method was climb-milling. The cutting tool employed in the experiment is an F2330.Z25 high-feed milling cutter (produced by Walter). During the experiment, the signal sensor was attached to the different surfaces of the workpiece along the X, Y, and Z directions. The vibration test system and vibration acceleration signal are shown in Figure 1b,c, and the cutter tooth was a P26339R14 indexable blade (produced by Walter), as shown in Figure 1d.

Table 1. Experimental scheme.

Cutting Velocity (m/min)	Spindle Speed (rpm)	Milling Depth (mm)	Feed Rate (mm/min)	Milling Width (mm)	Milling Stroke (m)
115	1143	0.5	500	16	0.5, 1.0, 1.5, 2.0

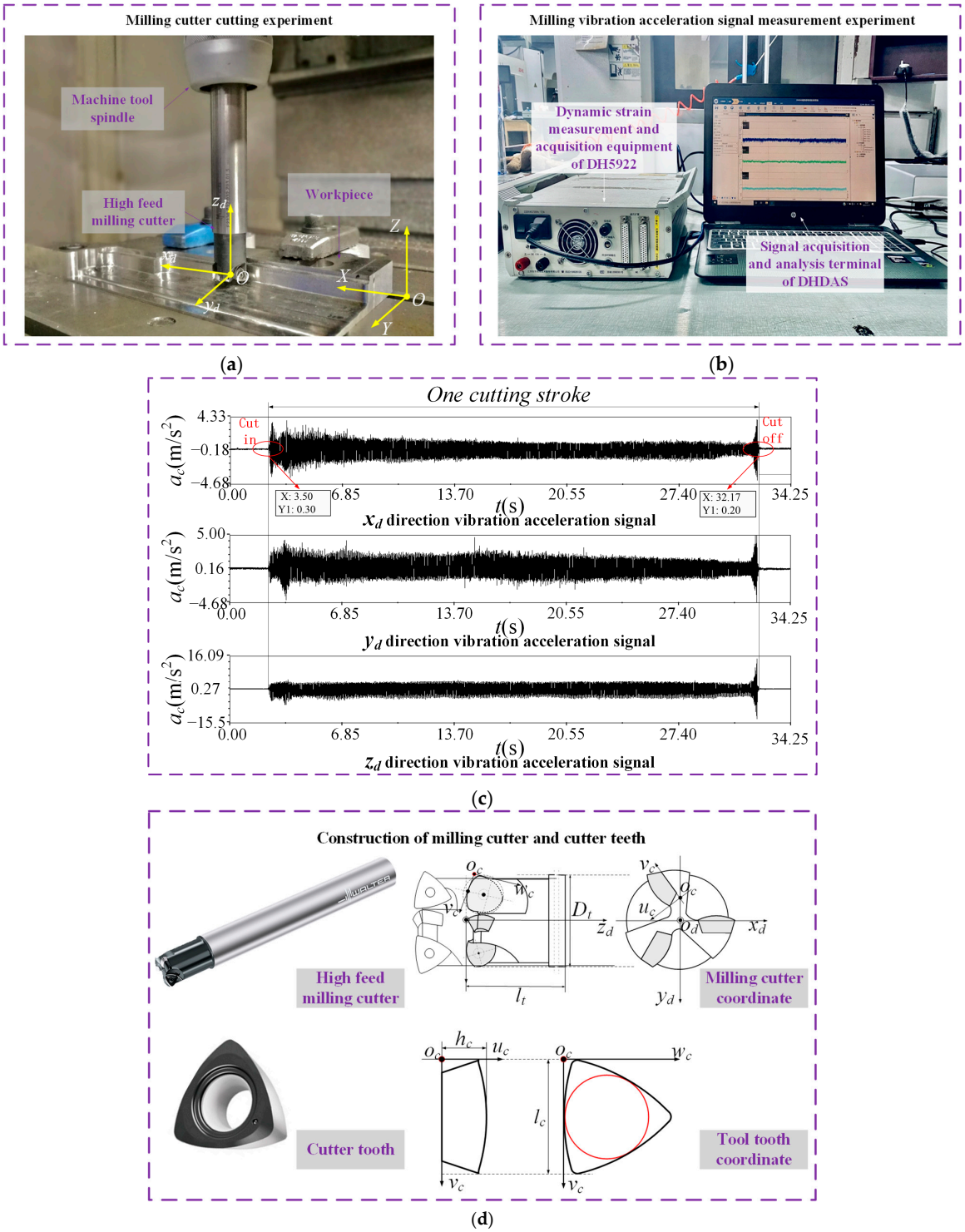


Figure 1. High-feed milling cutter: cutting and cutting acceleration signal measurement experiment. (**a**) Cutting experiment; (**b**) signal measurement experiment; (**c**) vibration acceleration signal; (**d**) milling cutter and cutter tooth construction.

In Figure 1a,d, *O-XYZ* is the workpiece co-ordinate system; o_c-$u_c v_c w_c$ is the co-ordinate system of the cutter tooth structure. The point o_c is a point on the intersection of the plane where the lowest point of the cutter tooth structure is located and the plane where the end face of the cutter tooth is located. The vertical line of the end face is taken as the projection surface along the *z*-axis direction of the workpiece. The u_c-axis passes through the intersection of the plane where the lowest point of the cutter tooth structure is located and the plane where the end face of the cutter tooth is located. o_d-$u_d v_d w_d$ is the milling cutter structure co-ordinate system; D_t is the tool diameter. L_t is the length of the milling cutter, l_c is the length of the cutter teeth, and h_c is the height of the cutter teeth.

The motion trajectory and attitude of the milling cutter and its cutter teeth directly affect the contact relationship between the cutter teeth and the workpiece, thus affecting the change in the contact stiffness and incremental wear of the flank. In order to reveal the dynamic tool–workpiece relationship under vibration, a dynamic cutting process model is established, as shown in Figure 2, and the material and structural parameters of the milling cutter and the workpiece are shown in Table 2.

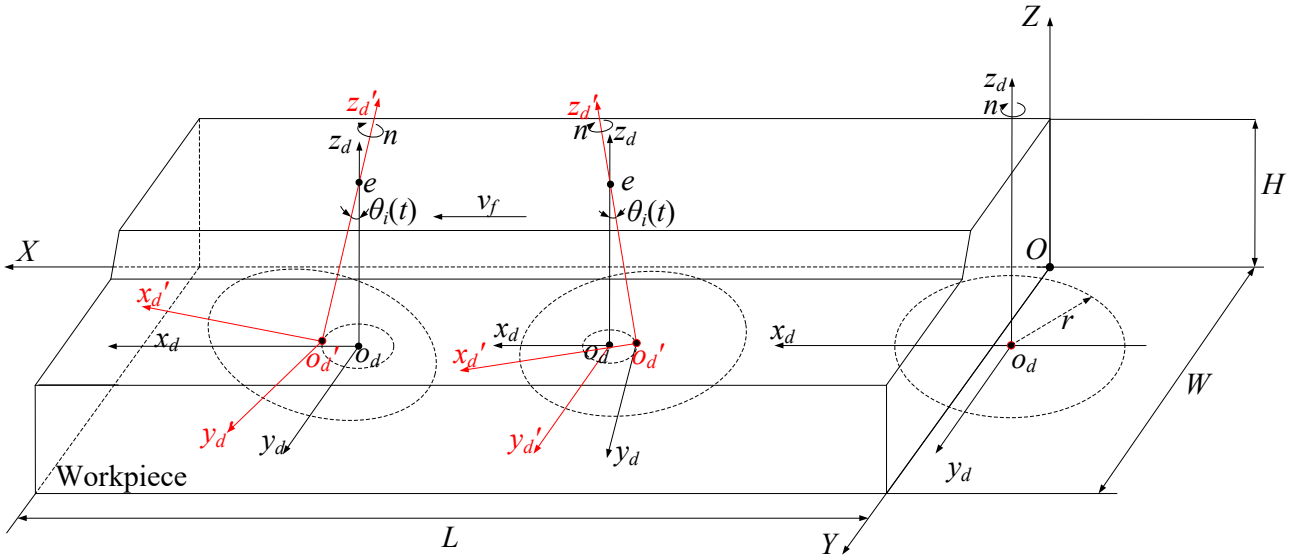


Figure 2. Dynamic cutting process of milling cutter under vibration.

Table 2. Material and structure parameters of milling cutter and workpiece.

Milling Cutter Materials	Coating Materials	Workpiece Materials	Workpiece Length *L* (mm)	Workpiece Width *W* (mm)	Workpiece Height *H* (mm)	Milling Cutter Diameter D_t (mm)	Milling Cutter Length l_t (mm)
WC	Ti-CN	Ti-6Al-4V	300	100	20	32	250

After determining the structure of the high-feed milling cutter and the structure of the cutter tooth, it is necessary to analyze the structure of the cutter tooth flank. The geometric model of the projection of the cutter tooth flank in the u_c-o_c-v_c direction in the cutter tooth co-ordinate system is given in Figure 3. Among them, the width of the flank projection is 10.7 mm, and the height is 3.98 mm. Make a dividing line along the vertical projection direction of the cutting edge of the cutter tooth, divide it into 42 equal-width distances on average, and make a dividing line parallel to the projection direction of the cutting edge.

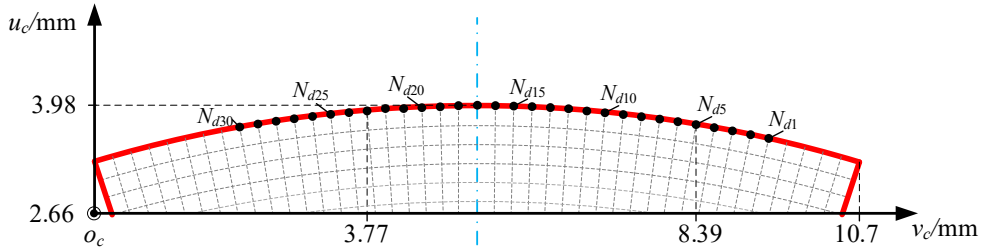


Figure 3. Selection position of cutting edge feature points on flank face.

In the cutting process, not all areas of the flank face are involved in the cutting. After data statistics, the flank face with a height range of 2.66–3.98 mm was selected for research. In the high-efficiency cutting processes, the main area of flank wear is concentrated near the cutting edge. Therefore, the position of the cutting edge is an important area for studying the wear of the flank face of the cutter tooth. A total of 30 wear characteristic points N_{di} (N_{d1}~N_{d30}) along the cutting edge direction on the flank face of the cutter tooth were selected and are shown in Figure 2.

3. Calculation of Instantaneous Contact Stiffness of Milling Cutter Tooth Flank under Different Deformation Conditions

Under the action of cutting vibration, the instantaneous contact state and surface morphology of the tool and the workpiece affect the instantaneous contact stiffness of the flank, which needs to be revealed. The instantaneous deformation of the flank under an external load will change. The change in the instantaneous contact stiffness of the flank under different deformation conditions was analyzed. It provides a basis for studying the distribution of instantaneous flank contact stiffness under vibration.

3.1. Calculation of Instantaneous Contact Stiffness in Elastic Deformation Stage

The elastic deformation, elastic–plastic deformation, and plastic deformation stages are represented by *e*, *ep*, and *p*, respectively.

When the external load is extremely small, the asperity on the flank only undergoes elastic deformation, and its micro-contact characteristics (average contact pressure p_e; stiffness k_e) can be solved by Hertz contact theory [31], expressed as

$$p_e = \frac{4E^*(\omega_e/r_t)^{\frac{1}{2}}}{3\pi} = k_v H_v \left(\frac{\omega_e}{\omega_{ec}}\right)^{\frac{1}{2}} \tag{1}$$

$$k_e = 2E^*{\omega_e}^{\frac{1}{2}}{r_t}^{\frac{1}{2}} = \frac{3}{2}k_v H_v \pi r_t \left(\frac{\omega_e}{\omega_{ec}}\right)^{\frac{1}{2}} \tag{2}$$

In the equation, ω_{ec} is the critical yield point; k_v is the average contact pressure factor.

$$k_v = \frac{2}{3}K_v \tag{3}$$

K_v is the maximum contact pressure factor.

$$K_v = 0.454 + 0.41\mu_a \tag{4}$$

In the equation: μ_a is Poisson's ratio; E^* is the equivalent elastic modulus of the contact material between the cutter tooth and the workpiece:

$$E^* = \left(\frac{1-{\mu_{a1}}^2}{E_1} + \frac{1-{\mu_{a2}}^2}{E_2}\right)^{-1} \tag{5}$$

In the equation, E is the elastic modulus of the milling cutter tooth material; h_v is the material hardness;

The solution of critical yield point ω_{ec} is

$$\omega_{ec} = \left(\frac{\pi K_v H_v}{2E^*}\right)^2 r_t \tag{6}$$

By substituting ω_{ec} into the above equation, the contact characteristics at the critical yield point of the flank can be obtained:

$$\begin{cases} p_{ec} = H_v k_v \\ S_{ec} = \pi r_t \omega_{ec} \\ F_{ec} = H_v k_v \pi r_t \omega_{ec} \\ K_{ec} = \frac{3}{2} H_v k_v \pi r_t \end{cases} \tag{7}$$

3.2. Calculation of Instantaneous Contact Stiffness in Complete Plastic Deformation Stage

According to the contact mechanics theory of Johnson [32], when the average contact pressure on the flank surface is equal to the yield strength of the cutter tooth material, the asperity on the cutter tooth undergoes complete plastic deformation. The contact characteristics can be solved by an AF fully plastic contact theory model (Abbotte Firestone). At this time, the deformation is ω_p, and the critical deformation is ω_{pc}:

$$\omega_{pc} = 110\omega_{ec} \tag{8}$$

The contact stiffness is

$$k_p = 2\pi H_v r_t \tag{9}$$

3.3. Instantaneous Contact Stiffness Calculation in Elastic-Plastic Deformation Stage

The contact characteristics (contact load F_{ep} and contact stiffness k_{ep}) in the elastoplastic deformation stage are:

$$F_{ep} = \frac{2}{3}\pi K_v H_v r_t \omega_{ec} \exp\left[C_1 \ln\left(\frac{\omega_{ep}}{\omega_c}\right) + C_2 \ln^2\left(\frac{\omega_{ep}}{\omega_c}\right) + C_3 \ln^2\left(\frac{\omega_{ep}}{\omega_c}\right) * \ln\left(\frac{\omega_{ep}}{\omega_p}\right)\right] \tag{10}$$

$$k_{ep} = \frac{F_{ep}}{\omega_{ep}} \times \left\{C_1 + 2C_2 \ln\left(\frac{\omega_{ep}}{\omega_c}\right) + C_3 \ln\left(\frac{\omega_{ep}}{\omega_c}\right) \times \left[2\ln\left(\frac{\omega_{ep}}{\omega_p}\right) + \ln\left(\frac{\omega_{ep}}{\omega_c}\right)\right]\right\} \tag{11}$$

$$C_1 = \frac{3}{2}, C_2 = \frac{\ln\frac{3q}{K_v} - \frac{3}{2}\ln q}{\ln^2 q}, C_3 = \frac{\frac{5}{2}\ln q - 2\ln\frac{3q}{K_v}}{\ln^3 q} \tag{12}$$

From Equations (2), (9), and (11), it can be seen that the instantaneous contact stiffness of the flank is not only affected by the positive pressure and deformation but also by the change in the asperity structure distributed on the flank, which will cause a change in the instantaneous contact stiffness. It shows that the instantaneous morphology of the flank will also change its variation characteristics, which leads to variability in the instantaneous contact stiffness of the flank. Therefore, the change in the instantaneous morphology of the flank will also cause a change in the instantaneous contact stiffness.

4. Characterization of Distribution of Instantaneous Contact Stiffness

The surface roughness varies continuously and is affected by material of cutter and workpiece, cutting vibration, and matching degree of cutter and workpiece during the cutting process. Meanwhile, with the increase in the cutting stroke, the coating on the milling cutter teeth will gradually fall off and wear the milling cutter, thus affecting the processing quality.

The structure of the milling cutter and the structure of the cutter teeth will affect the construction of the equation for the flank of the cutting edge and the milling cutter teeth, thus affecting the construction of a contact stiffness model of the cutter–workpiece contact surface and then, in turn, affecting the calculation of the posture of the flank friction and wear area elements and the establishment of the structure for processing the transition surface. In order to illustrate the dynamic properties of the instantaneous processing of the state of friction and wear area element transition surface on the cutter flank under vibration, the design process of the distribution profile of the instantaneous stiffness on the flank is shown in Figure 4.

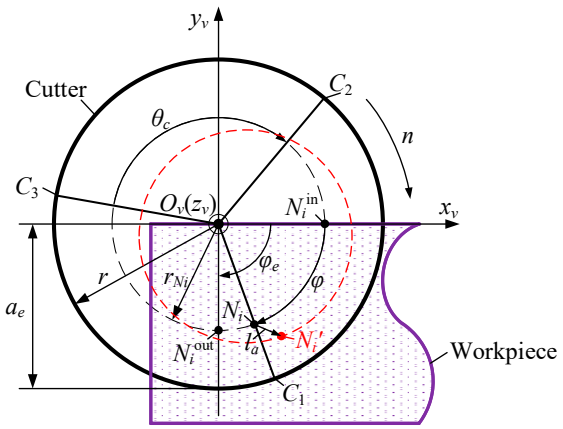


Figure 4. Design process of the distribution profile of instantaneous stiffnesses on the flank.

In Figure 4, *O-XYZ* is the co-ordinate system of the workpiece; o_v-$x_v y_v z_v$ is the structural co-ordinate system of the milling cutter, point o_v is the intersection of the milling cutter axis and the plane where the lowest point of the cutter teeth is located; axis x_v is in the plane where the lowest point of the tooltip is located and perpendicular to the y_v axis; axis y_v is in the plane where the lowest point of the tooltip is located and the point at which the tool tip has the maximum diameter; o_v'-$x_v' y_v' z_v'$ is the structure co-ordinate system of the milling cutter under vibration; C_1, C_2, and C_3 represent cutter tooth 1, cutter tooth 2, cutter tooth 3, respectively. φ is the instantaneous rotation angle of the cutter tooth; φ_e is the effective cutting angle of the cutter tooth, $\varphi_e = 90°$; θ_c is the included angle between two cutter teeth; N_i is an arbitrary point on the flank face without vibration; N_i' is an arbitrary point on flank face of a cutter tooth when N_i is vibrating; l_a is the vibration displacement of N_i; N_i^{in} is the co-ordinate point when an arbitrary point on the cutting edge cutting into the workpiece; N_i^{in} is the co-ordinate point where an arbitrary point on the cutting edge finishes effectively cutting; r_{Ni} is the gyration radius of an arbitrary point on the cutting edge.

After using MATLAB (2021a) software to calculate the instantaneous contact stiffness, the Origin (2022b) software was used to draw the distribution state of the instantaneous contact stiffness of the flank. The distribution of the instantaneous contact stiffness on the flank over six cycles of the high-feed milling cutter cutting a workpiece is given in Figures 5–7. Six instantaneous moments with a milling cutter rotation angle of 15°, 30°, 45°, 60°, 75°, and 90° were selected to study the distribution properties of the instantaneous contact stiffness of the cutter flank at different times under different cycles.

From Figures 5–7, it is observed that in the axial direction of the flank, the instantaneous contact stiffness is mainly concentrated near the cutting edge. With the increase in milling cutter rotation angle, the instantaneous contact stiffness area first increases and then decreases. Similarly, with the increase in milling cutter rotation angle, the instantaneous contact stiffness value also shows a trend of increasing first and then decreasing. The results of the instantaneous contact stiffness distribution on the flank of the high-feed milling cutter show that, although the cutting cycles are not continuous with each other and the time

span is large, the instantaneous contact stiffness distribution presents similar laws. In the same cutting cycle, the contact stiffness is mainly concentrated in the middle of the cutting edge. With the increase in tooth rotation angle, the contact stiffness gradually accumulates until the tooth rotation angle φ reaches the maximum value, which is around 45°, and then the stiffness decreases. These phenomena are the coupling results of pressure, strain, and strain rate between the cutter flank and the workpiece at the processing transition surface. The instantaneous contact stiffness is not uniformly distributed along the cutting area of the cutter tooth, and there is a high value near v_c, which is 6~8 mm. With the increase in cutter tooth rotation angle, it can be observed that the peak value of instantaneous contact stiffness moves from the outside to the inside of the cutting edge. The increase in cutter tooth rotation angle mainly affects the increase in the strain rate in the cutting deformation zone. As mentioned earlier, the strain rate affects the change in stiffness by affecting the deformation of the deformation area of the flank. The higher the strain rate, the greater the instantaneous contact stiffness.

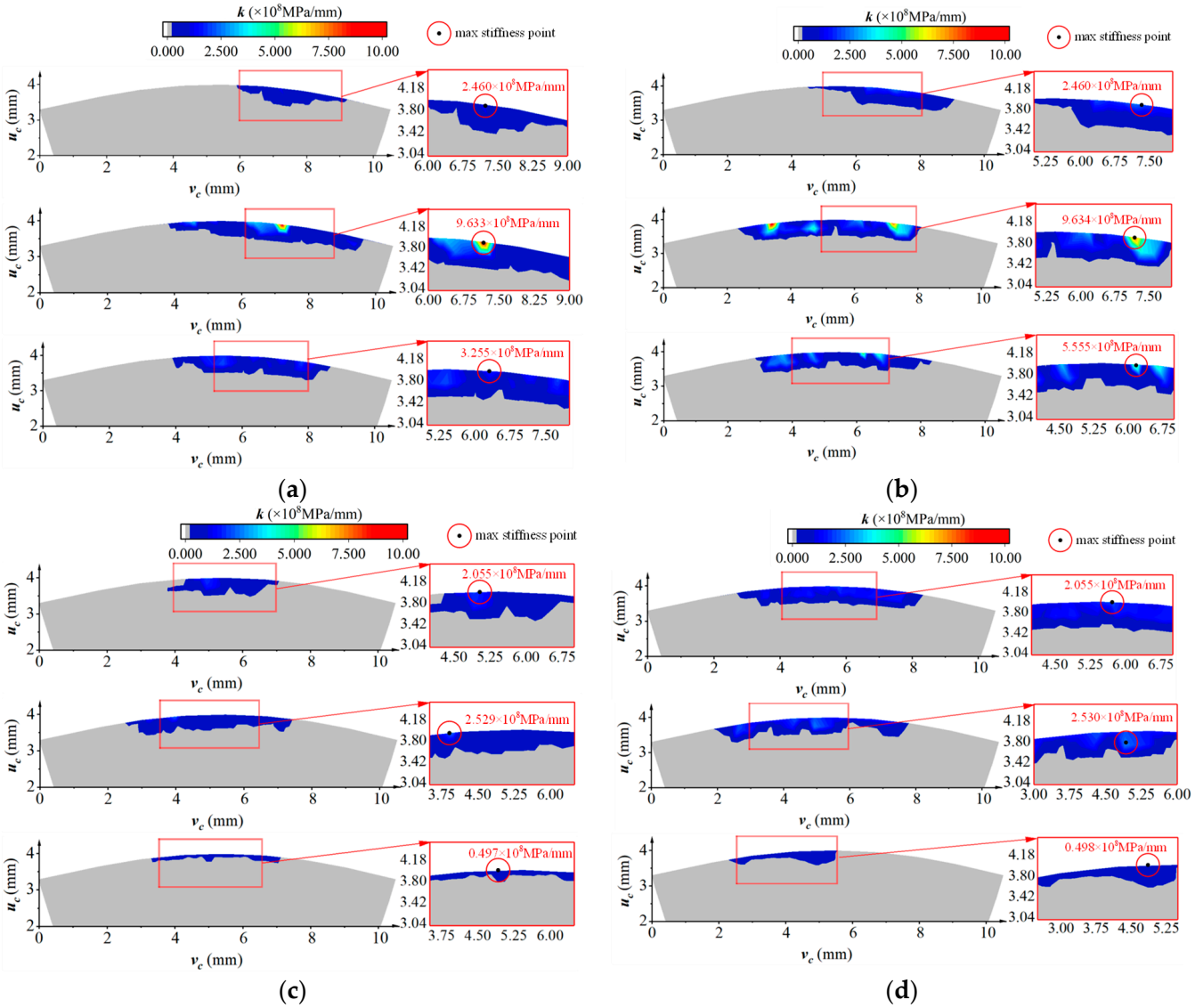


Figure 5. Distribution of the instantaneous contact stiffness of the cutter flank of T_1 and T_2. (**a**) Distribution of stiffness of cycle T_1 when φ is 15°, 30°, and 45°. (**b**) Distribution of stiffness of cycle T_2 when φ is 15°, 30°, and 45°. (**c**) Distribution of stiffness of cycle T_1 when φ is 60°, 75°, and 90°. (**d**) Distribution of stiffness of cycle T_2 when φ is 60°, 75°, and 90°.

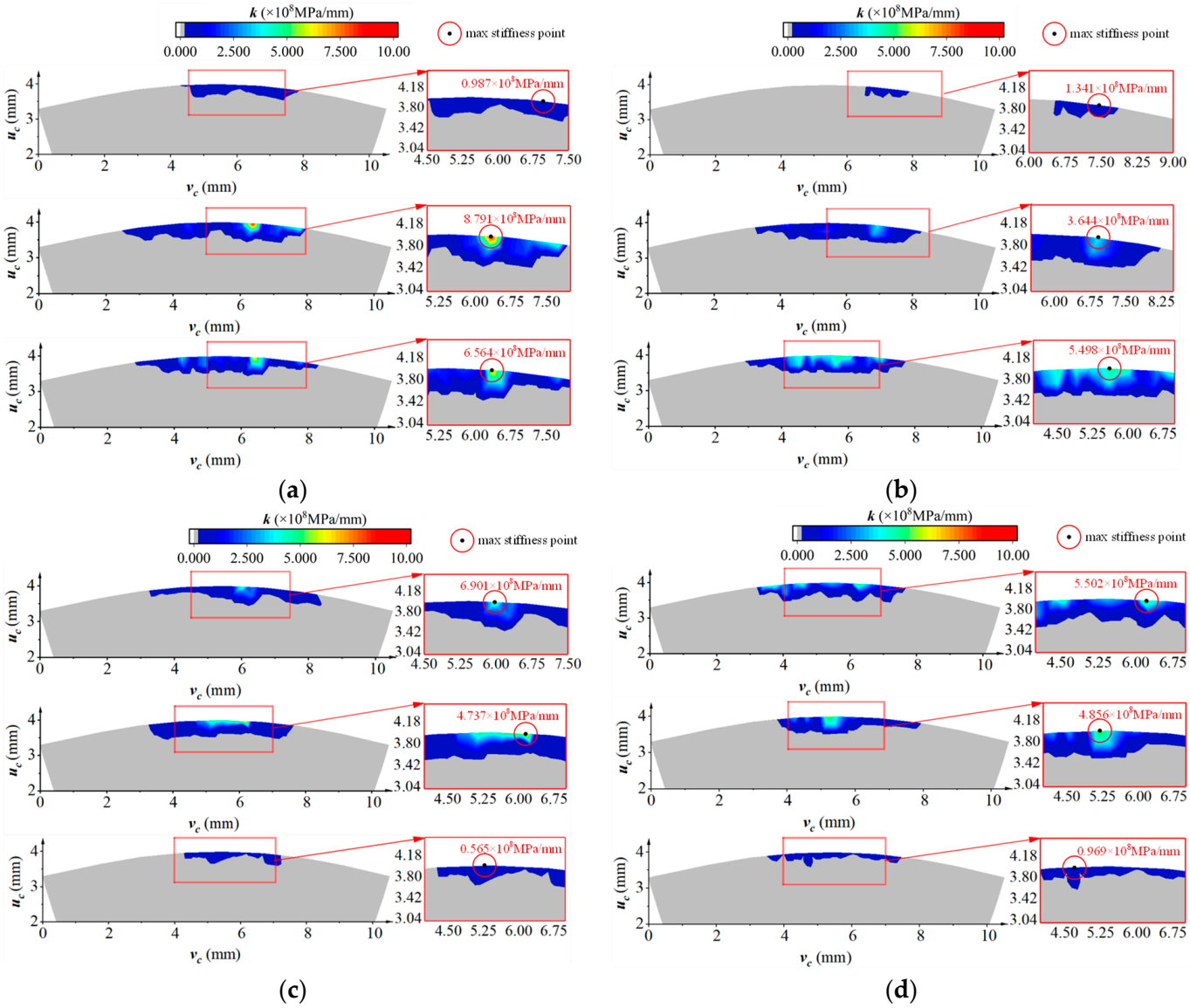


Figure 6. Distribution of instantaneous contact stiffness of the cutter flank of T_3 and T_4. (**a**) Distribution of stiffness of cycle T_3 when φ is 15°, 30°, and 45°. (**b**) Distribution of stiffness of cycle T_4 when φ is 15°, 30°, and 45°. (**c**) Distribution of stiffness of cycle T_3 when φ is 60°, 75°, and 90°. (**d**) Distribution of stiffness of cycle T_4 when φ is 60°, 75° and 90°.

In each cutting cycle, whether in the transverse direction (along the cutting edge direction) or the longitudinal direction (along the axial direction of the flank) of the flank, the distribution of the instantaneous contact stiffness of the cutter flank is related to the cutting area. When the rotation angle is 0~30°, the instantaneous contact stiffness is concentrated around the speed when v_c is 7 mm outside of the cutting edge. The distribution area is small, and the contact stiffness value is small when the rotation angle is 0~15° (the maximum is 0.86 × 10^{-8} MPa); the value increases significantly when the rotation angle is 15°~30°. When the rotation angle is 30°~60°, the distribution area of the instantaneous contact stiffness is the largest, and the peak value of the contact stiffness in each cutting cycle will also appear in this period (the maximum is 10.2 × 10^{-8} MPa). When the rotation angle is 60°~90°, the instantaneous contact stiffness is concentrated around the speed when v_c is 5 mm on the inner side of the cutting edge, and with the increase in the rotation angle, the stiffness distribution area decreases, and the instantaneous contact stiffness value gradually decreases.

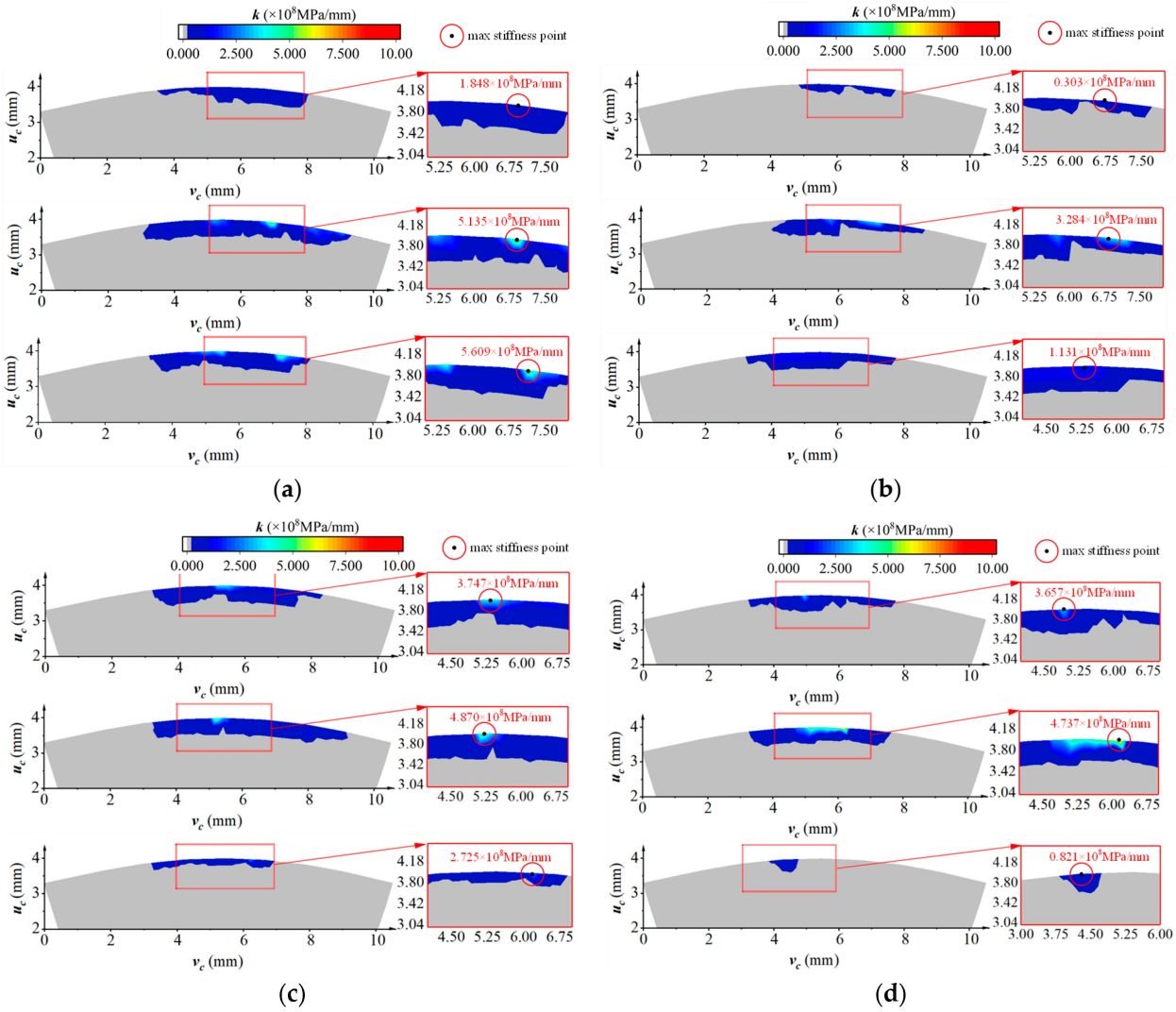


Figure 7. Distribution of instantaneous contact stiffness of cutter flank of T_5 and T_6. (**a**) Distribution of stiffness of cycle T_5 when φ is 15°, 30°, and 45°. (**b**) Distribution of stiffness of cycle T_6 when φ is 15°, 30°, and 45°. (**c**) Distribution of stiffness of cycle T_5 when φ is 60°, 75°, and 90°. (**d**) Distribution of stiffness of cycle T_6 when φ is 60°, 75°, and 90°.

5. Characterization of Distribution State of Wear Depth

The calculation method of the increment in wear generated on the flank is given as the following [33]:

$$\Delta = a \int pV_\tau \exp(-\frac{b}{T})dt \tag{13}$$

In the equation, V_τ is the slipping velocity; T is the interface temperature (absolute degree); dt is the time increment; a is the mechanical coefficient; b is the temperature coefficient.

In order to study the influence of stiffness on the increment in wear on the flank of the high-feed milling cutter, it is necessary to analyze the instantaneous increment in wear distribution on the flank. The least square method was used to interpolate and fit the incremental wear distribution of the flank, and the milling cutter rotation angle in the same cycle was selected based on the distribution change in the instantaneous contact stiffness of the flank of the cutter in a cutting cycle in Section 3. The distribution of the increment in wear at the rotation angle φ is 30°, 45°, and 60°, and the images of the instantaneous wear depth distribution of the flank of the cutter tooth changing with time in a cutting cycle were obtained as shown in Figure 8.

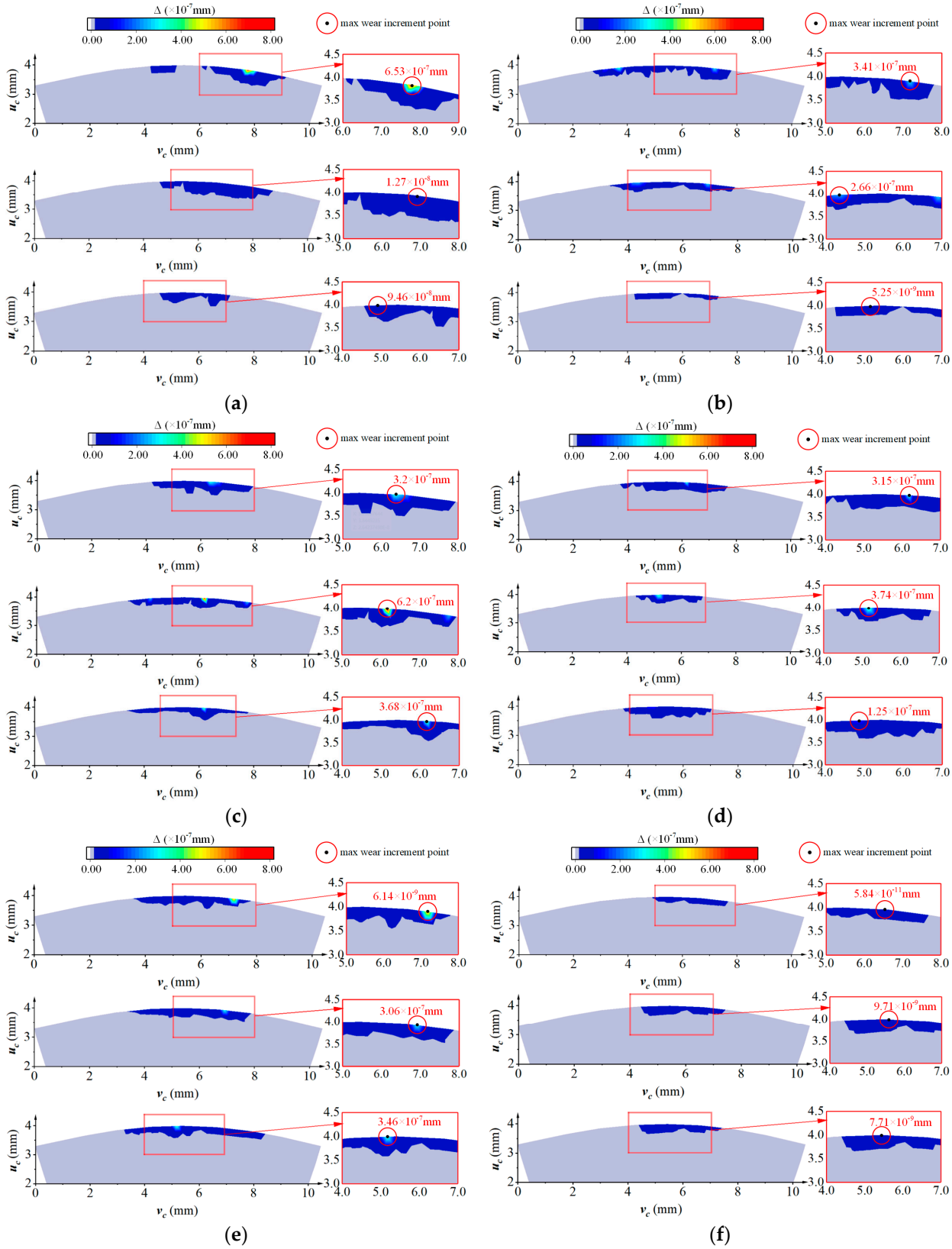


Figure 8. Instantaneous incremental wear distribution of flank face of T_1 to T_6 periodic cutter. (**a**) Stiffness distribution at cycle T_1 when φ is 30°, 45°, and 60°; (**b**) Stiffness distribution at cycle T_2 when φ is 30°, 45°, and 60°; (**c**) Stiffness distribution at cycle T_3 when φ is 30°, 45°, and 60°; (**d**) Stiffness distribution at cycle T_4 when φ is 30°, 45°, and 60°; (**e**) Stiffness distribution at cycle T_5 when φ is 30°, 45°, and 60°; (**f**) Stiffness distribution at cycle T_6 when φ is 30°, 45°, and 60°.

Similar to the instantaneous contact stiffness of the flank, the distribution of the incremental wear and the contact stiffness are in the same area, and the main wear area is also the same as the main instantaneous contact stiffness, with both concentrated near the cutting edge. With the increase in the milling cutter rotation angle, the wear area first increases and then decreases; similarly, with the increase in the milling cutter rotation angle, the value of instantaneous incremental wear also shows a trend of first increasing and then decreasing.

The influential mechanism on wear distribution can be understood as follows: on the one hand, when the rotation angle of the tool increases, the milling cutter spindle moves along the cutting direction, which leads to the transition of the wear area from the outside of the cutting edge direction to the inside of the cutter tooth. On the other hand, with the increase in the rotation angle of the milling cutter, the accumulation of chips and the change in shear angle cause the incremental wear value to decrease from small to large.

After extracting and calculating the instantaneous contact stiffness and incremental wear data of the flank face, the improved grey correlation degree analysis algorithm was used to calculate the correlation between the contact stiffness and the increment in wear [34]. The results are shown in Table 3.

Table 3. Grey correlation degree between contact stiffness and incremental wear of the flank at the same time.

$\varphi \backslash T$	T_1	T_2	T_3	T_4	T_5	T_6
15°	0.7805	0.6894	0.6797	0.7329	0.9012	0.9161
30°	0.7873	0.6213	0.7132	0.7851	0.7471	0.7289
45°	0.6528	0.8552	0.6644	0.88	0.6833	0.6616

According to Table 3, the minimum correlation degree is 0.6213 in the correlation degree calculation results, and the remaining correlation degree calculation results are all above 0.65, with all being greater than 0.5 and so belonging to a strong correlation. At the same time, the correlation between the contact stiffness and the increment in wear of the flank is high, indicating that the distribution of the contact stiffness and the incremental wear on the flank have similar variation characteristics with time.

In order to study the wear evolution process of the flank, the change in the wear depth d_t of the flank with the cutting stroke L_g was plotted using the color scale diagram. Select 25 wear feature points $N_{di}(N_{d1}$~$N_{d25})$ on the flank along the cutting edge direction as shown in Figure 9, study their wear depth change characteristics when the cutting stroke is 0~0.5 m, and draw the profile of the flank wear depth when the cutting stroke L_g is 0.125 m, 0.25 m, 0.375 m, and 0.5 m.

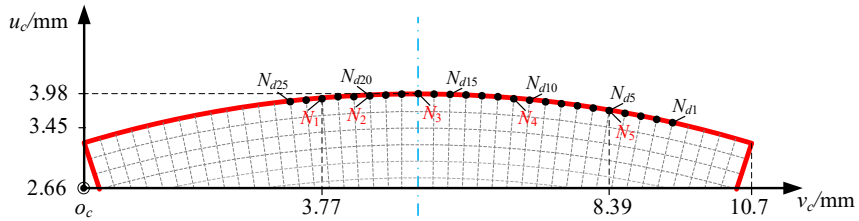


Figure 9. Feature points of flank wear depth.

In Figure 10, L_g is the cutting stroke of the milling cutter; the value range is [0,0.5], and the unit is m; $d_{0.5}$ is the wear depth when the cutting stroke is 0.5 m, that is, the wear depth at the end of the cutting stroke; d_r is the wear rate:

$$d_r = \frac{d_t^{\text{last}}}{L_g^{\max}} \tag{14}$$

where d_t^{last} is the wear depth at the end of the cutting stroke; $L_g^{\max}$ is the maximum cutting stroke.

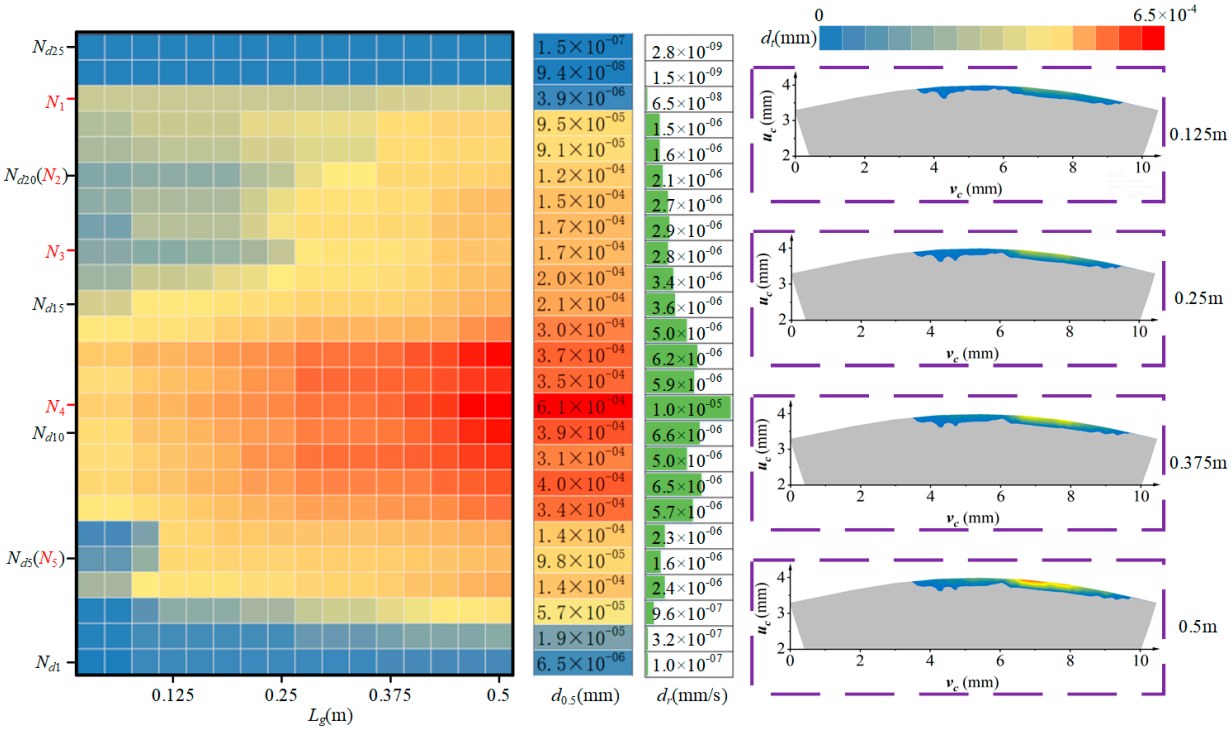


Figure 10. Variation in wear depth d_t with cutting stroke L_g.

It can be seen from Figure 10 that the wear depth d_t of different wear feature points varies with the cutting stroke L_g. From the overall distribution, although the wear rate is different, the wear depth of all selected points changes with the increase in cutting stroke, indicating that there is no accidental wear at the selected points. Among them, the wear depth of the selected points at both ends is the smallest. When the cutting stroke is 0.5 m, the wear depth of N_{d1} is $d_t = 6.51 \times 10^{-6}$ mm, and the wear depth of N_{d25} is $d_t = 1.52 \times 10^{-7}$ mm; The wear rate d_r is 1.08×10^{-7} mm/s and 2.53×10^{-9} mm/s, accounting for only 0.02% and 1.08% of the maximum wear rate. The maximum wear area is between N_{d5} and N_{d15}, and the wear depth d_t is about 4×10^{-4} mm, which indicates that the main wear area on the flank is relatively concentrated; the maximum wear depth of the flank is $N_{d11}(N_4)$, its wear depth $d_t = 6.07 \times 10^{-4}$ mm, followed by N_{d8} and N_{d10}, and this shows a decreasing trend towards both ends. The position of the feature point N_{d11} is not near the edge of the cutting area (N_{d11} and N_{d23}) nor near the central axis of the flank (N_{d17}). The wear depth d_t of N_{d11} is the largest, which is due to the extrusion deformation of the transition surface and the shear deformation when the cutting edge shears the workpiece at the same time, which is the same as the concentration of the instantaneous contact stiffness of the flank of the cutter tooth.

Based on the above analysis, there is a restriction on the distribution of the instantaneous contact stiffness and incremental wear on the flank of the cutter tooth: the geometric structure of the cutter tooth itself. The shape of the cutting edge and flank is the fundamental reason for the change in contact state between the cutter tooth and workpiece, which also leads to the obvious change in contact stiffness and incremental wear with the rotation angle of the cutter tooth.

6. Wear Prediction of Flank Face of Cutter Tooth

The effective decision-making for tool wear status monitoring research is provided by the development of artificial intelligence, and neural networks are used as the common

method [35–39]. Currently, the BP neural network is the most widely used decision-making model in the field of tool wear status monitoring [40].

6.1. Back Propagation Neural Network

The core of the BPNN (back propagation neural network) is to update the weights through error post-term propagation and gradient decrement to find the best result for the entire path. When predicting the incremental flank wear, the BPNN can be trained with a certain number of training samples to fit the relationship between the incremental flank wear and the milling parameters under specific machining conditions. According to the basic principle of a BPNN, compared with the multiple-hidden-layer structure, the single hidden layer is simpler and has better characteristics for fitting nonlinear functions. Therefore, the single-hidden-layer BPNN prediction model constructed in this paper is shown in Figure 11.

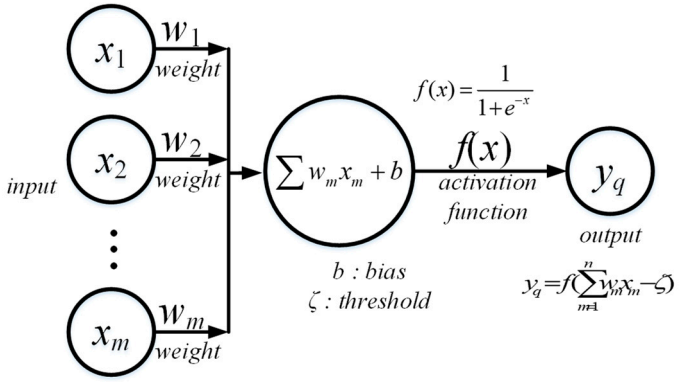


Figure 11. Single-hidden-layer BPNN prediction model.

6.2. Learning Process of BPNN

(1) First assign random numbers to each connection weight in the BPNN. Then, the function calculation accuracy ε and the maximum number of learning events M are given, and this stops when the number of learning events exceeds M; the error is set to e.

(2) Then, set the input sample of the randomly selected neuron network as x, the number of input samples for wear prediction as m, the predicted value of output incremental wear as y, the expected output incremental wear as d, the number of output incremental wear samples is n when the lth input sample is randomly selected, which can be expressed as

$$x(l) = (x_1(l), x_2(l), x_3(l), \cdots x_m(l)),\ l = 1, 2, \cdots m \tag{15}$$

$$d(l) = (d_1(l), d_2(l), d_3(l), \cdots d_n(l)) \tag{16}$$

(3) The transfer function used by the BPNN to calculate the incremental flank wear of the cutter tooth is the Sigmoid function (S function). If there is any input, then any output is

$$\text{out} = f(\text{in}) = \frac{1}{1 + e^{-\text{in}}} \tag{17}$$

$$f'(\text{in}) = \frac{1}{1 + e^{-\text{in}}} - \frac{1}{(1 + e^{-\text{in}})^2} = \text{out}(1 - \text{out}) \tag{18}$$

When setting the input of the hidden layer of the neural network to h^{in}, the number is i, the output of the hidden layer is h^{out}, the number is j, the input of the output layer is y^{in},

and the output of the output layer is y^{out} when the lth flank wear prediction input sample is randomly selected:

$$h_i^{\text{in}}(l) = \sum_{o=1}^{m} w_{oi} x_o(l) - b_i, i = 1, 2, \cdots p \tag{19}$$

$$h_i^{\text{out}}(l) = f\left(h_i^{\text{in}}(l)\right) \tag{20}$$

$$y_j^{\text{in}}(l) = \sum_{o=1}^{p} w_{ij} h_i^{\text{out}}(l) - b_j, j = 1, 2, \cdots q \tag{21}$$

$$y_j^{\text{out}}(l) = f\left(y_j^{\text{in}}(l)\right) \tag{22}$$

(4) With w as the weight, finding the partial derivative δ_j of the error function with respect to the neurons in the output layer by using the expected incremental wear output value and the actual incremental wear output value of the BPNN when the lth input sample is randomly selected, means

$$\frac{\partial e}{\partial w_{ij}} = \frac{\partial e}{\partial y_j^{in}} \frac{\partial y_j^{in}}{\partial w_{ij}} \tag{23}$$

$$\frac{\partial e}{\partial y_j^{\text{in}}} = -\left(d(l) - y_j^{\text{out}}(l)\right) f'\left(y_j^{\text{in}}(l)\right) - \delta_j(l) \tag{24}$$

$$\frac{\partial y_j^{\text{in}}}{\partial w_{ij}} = \frac{\partial\left(\sum_{i}^{p} w_{ij} h_i^{\text{out}}(l) - b_j\right)}{\partial w_{ij}} = h_i^{\text{out}}(l) \tag{25}$$

(5) If calculating the partial derivative of the error function of the neurons in the hidden layer, then

$$\frac{\partial e}{\partial h_i^{\text{in}}} = -\left(\sum_{j=1}^{q} \delta_j(l) w_{ij}\right) f'\left(h_i^{\text{in}}(l)\right) - \delta_i(l) \tag{26}$$

(6) Update weights. The connection weight $w_{ij}(l)$ is corrected by the partial derivative of each neuron in the output layer and the output value of each neuron in the hidden layer in the BPNN.

$$\Delta w_{ij}(l) = -\eta \frac{\partial e}{\partial w_{ij}} = \eta \delta_j(l) h_i^{\text{out}}(l) \tag{27}$$

$$w_{ij}^{N+1} = w_{ij}^{N} + \eta \delta_j(l) h_i^{\text{out}}(l) \tag{28}$$

In the equation, η is the learning rate, $0 < \eta < 1$. The partial derivative of each neuron in the hidden layer and the input of each neuron in the input layer are used to adjust the connection weight.

$$\Delta w_{oi}(l) = -\eta \frac{\partial e}{\partial w_{oi}} = \delta_i(l) x_o(l) \tag{29}$$

$$w_{oi}^{N+1} = w_{oi}^{N} + \eta \delta_i(l) x_o(l) \tag{30}$$

According to the negative gradient direction of the error function, the connection weights and deviations between the hidden layer and the output layer of the BPNN are updated.

(7) When calculating the global error E_a:

$$E_a = \frac{1}{2M} \sum_{l=1}^{M} \sum_{j=1}^{q} \left(d_j(l) - y_j(l)\right)^2 \tag{31}$$

(8) Judging whether the error is up to standard.

During network training, the weights and thresholds are constantly adjusted to reduce the network error to a preset minimum value or to reach the maximum number of training stops. The predicted samples are input into the trained network to get the predicted results. If the above conditions are not met, the network will select the next learning sample and the corresponding expected output, return to (3), and proceed to the next exercise until the requirements are met.

6.3. Validation of the Predictive Model for Flank Wear

When considering the generalization ability of the BPNN, this research chooses the 5-1-1 structure for the neural network. There are six main factors affecting the wear of the cutter tooth: contact stiffness k, flank feature point co-ordinates (u_c, v_c, w_c), milling cutter rotation angle φ, and vibration displacement l_a, as shown in Equation (32). Therefore, the number of input layer nodes is 6, the number of output layers is 1, and P_k is set as the input layer set of the neuron network. The correct selection of the number of neurons and activation functions in the hidden layer significantly affects the effectiveness of predicting tool wear. If the number of neurons is too large, the training time of the model will be extremely long and the error will be large. Conversely, if the number of neurons is extremely small, the generalization ability and fault tolerance of the model will be reduced.

$$P_k = \{k, u_c, v_c, w_c, \varphi, l_a\} \tag{32}$$

The training parameters of the neural network flank-wear-prediction model are set as follows: the maximum number of training events is 1000, the learning efficiency is 0.01, and the target mean square error (MSE) is 1×10^{-5}. After a lot of training, the unoptimized BPNN repeatedly falls into the local optimal solution and stops training when the number of training times or the target MSE is reached.

After determining the parameters of the BPNN, 600 sets of test data obtained from the tool wear test were used as network training and verification samples. In the MATLAB software (version 2022a), we used the rand function to randomly select 500 sets of data from the 600 sets in the table as the network training samples. Before network training, we used the maximum mapping function in the MATLAB toolbox to normalize the test data. This process can reduce the errors caused (by different orders of magnitude and dimensions), avoid neuron saturation, and improve the convergence speed of the neural network [41].

The MATLAB neural network toolbox is used, as shown in Figure 12. The BPNN can achieve the target MSE. When the test data is in the 67th iteration, the accuracy of the algorithm meets the optimal requirement of setting error.

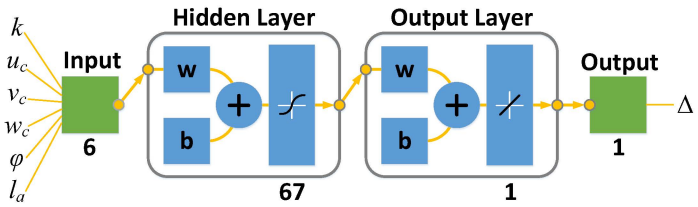


Figure 12. MATLAB neural network toolbox.

The instantaneous contact stiffness k, the flank feature point co-ordinates (u_c, v_c, w_c) of the cutter tooth co-ordinate system, the instantaneous rotation angle φ of the cutter tooth, and the vibration displacement l_a are taken as a group of inputs, and the instantaneous incremental wear is taken as a group of outputs. Among the 600 groups of signals, 500 groups were randomly selected as the training set for BPNN flank-wear-prediction training, and the remaining 100 groups of signals were used as the test set and verification set for BPNN flank-wear prediction. The prediction results are as follows:

In order to train the proposed BPNN neuron learning model and verify its effectiveness, all the schemes were verified, and the curves of the BPNN flank-wear prediction training set and test set were obtained. As shown in Figures 13 and 14, the abscissa is the training sample number, and the ordinate is the instantaneous amount of wear.

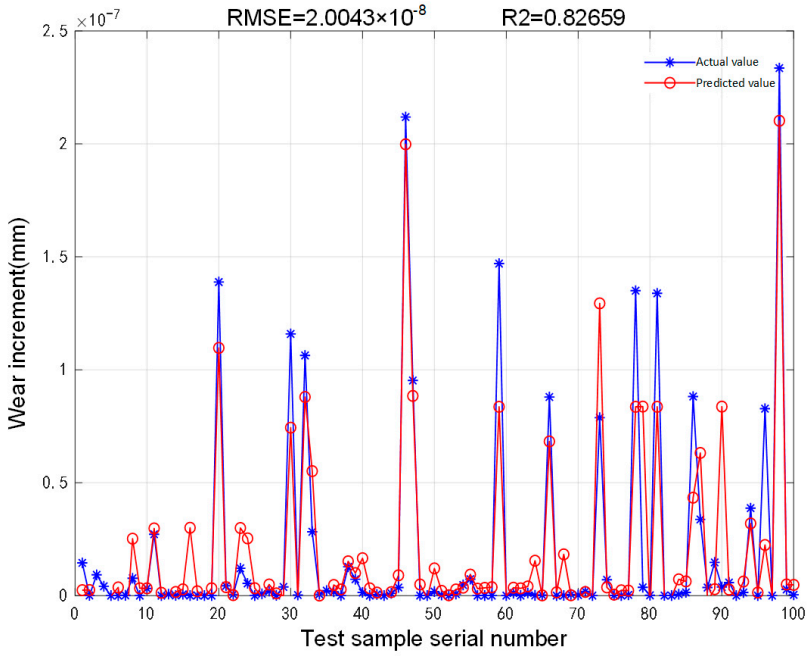


Figure 13. BPNN flank wear test set.

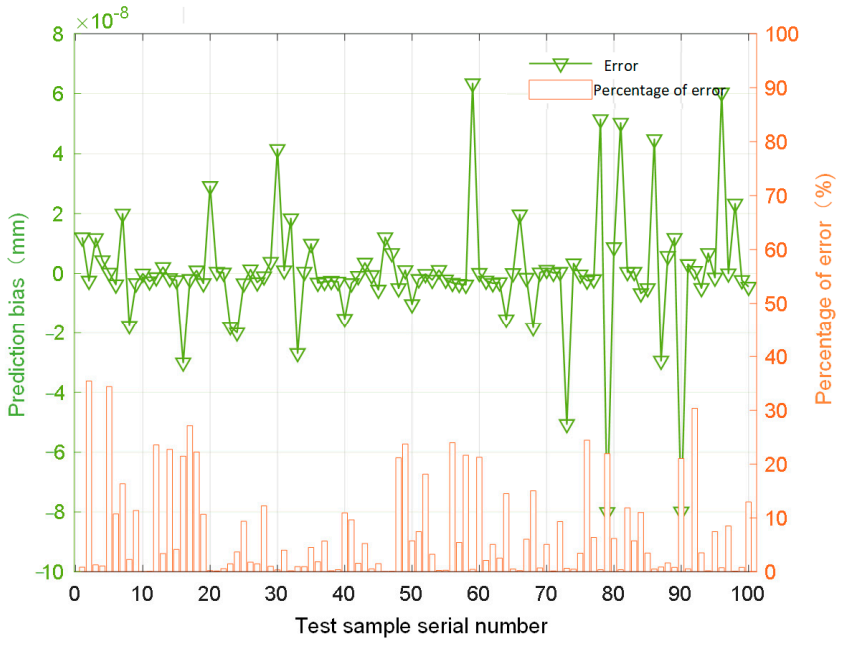


Figure 14. BPNN wear training set test error.

As shown in Figures 13 and 14, the instantaneous incremental wear of 100 test points is basically consistent with the actual incremental wear. Overall, the deviations between the predicted values of the instantaneous wear at the 100 test points and the measured values are all within 1×10^{-8} mm. The results show that the method has good prediction accuracy regarding incremental wear.

Through the response analysis of the normalization, the normalized response of the output layer of each subset of the BPNN flank-wear prediction can be obtained, as shown here:

Among them, $Tar_{max} = 1$; $Tar_{min} = -1$.

As can be seen from Figure 15, the distribution and similarity of the subsets do not differ significantly when compared to the normalized form. The similarity in Kr between the actual value Tar of the training set and the output value Val is 0.92559; the similarity in Kr between the actual value Tar of the verification set and the predicted value Val is 0.86433; the similarity in Kr between the actual value Tar of the test set and the predicted value Val is 0.8848; all similarities are greater than 0.8, which proves that the normalized response of each subset output layer has a good convergence effect, and the overall similarity in Kr between the actual value Tar and the predicted value Val is 0.9145 > 0.8.

$$Tar = \frac{(Tar_{max} - Tar_{min})(\Delta_i - \Delta_{min})}{\Delta_{max} - \Delta_{min}} + Tar_{min} \quad (33)$$

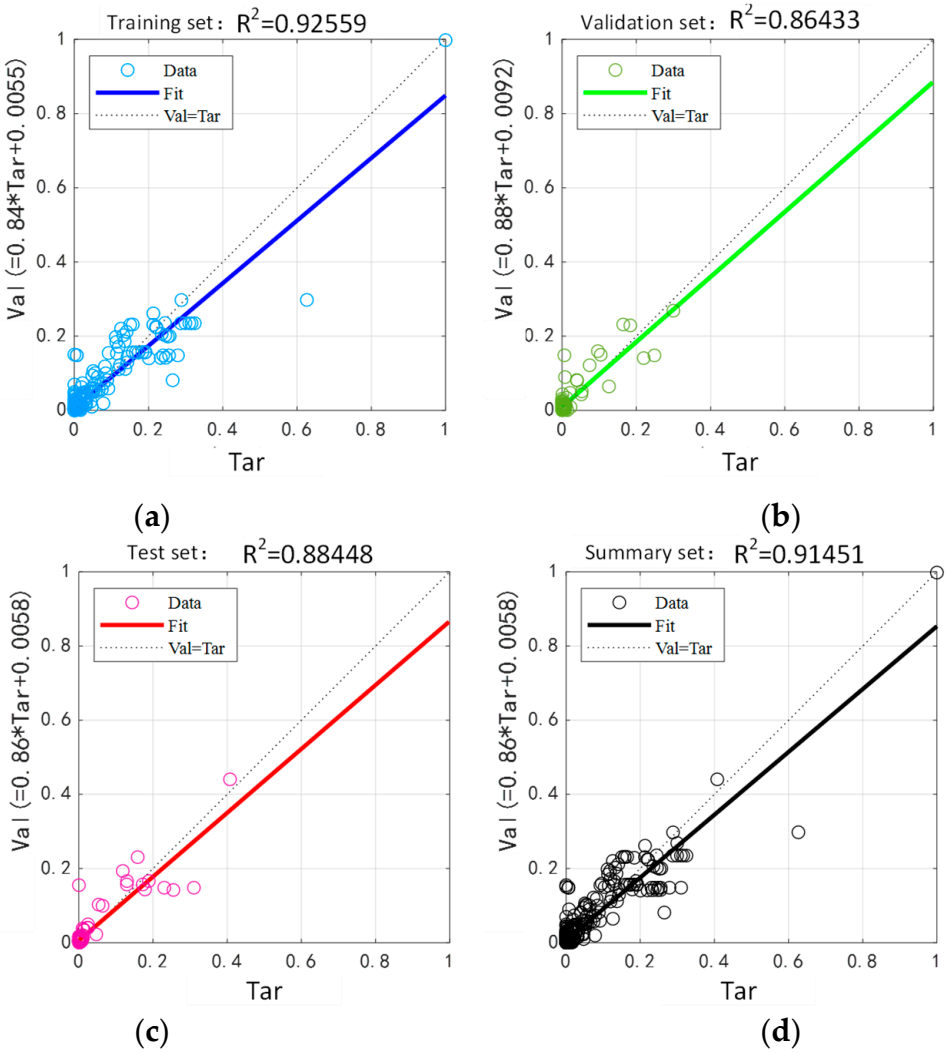


Figure 15. BPNN wear prediction normalized response of each subset output layer. (**a**) Training set; (**b**) validation set; (**c**) test set; (**d**) summary set.

The four statistical indexes, MSE, MAE, RMSE, and R^2, were used as the evaluation criteria for the accuracy of the BPNN to predict the instantaneous wear model of the cutter tooth flank, as shown in Table 4. The results are shown in Table 5.

Table 4. Statistical indicators and their calculation methods and characteristics.

Name	Calculation Methods and Characteristics
Square sum of residuals	$\mathrm{SSR} = \sum_{i=1}^{q} w_{ij}(y_j - y_j^{\mathrm{out}})^2$ (34)
	To calculate the sum of the square of the difference between the actual value and the predicted value of the flank incremental wear of the cutter tooth.
Total sum of square	$\mathrm{SST} = \sum_{i=1}^{q} w_{ij}(y_j - \overline{y})^2$ (35)
	It reflects the dispersion of all predicted value errors.
Regression sum of squares	$\mathrm{SSE} = \sum_{i=1}^{q} w_{ij}(y_j^{\mathrm{out}} - \overline{y})^2$ (36)
	It reflects the fitting of multivariate linear regression lines to sample observations.
Mean square error	$\mathrm{MSE} = \frac{\mathrm{SSR}}{m} = \frac{1}{m}\sum_{i=1}^{q} w_{ij}(y_j - y_j^{\mathrm{out}})^2$ (37)
	The difference between the actual value and the predicted value is reflected.
Mean absolute error	$\mathrm{MAE} = \frac{1}{m}\sum_{i=1}^{q} w_{ij}\left\lvert y_j - y_j^{\mathrm{out}}\right\rvert$ (38)
	The offset between different errors could be avoided.
Root mean square error	$\mathrm{RMSE} = \sqrt{\mathrm{MSE}} = \sqrt{\frac{1}{m}\sum_{i=1}^{q} w_{ij}(y_j - y_j^{\mathrm{out}})^2}$ (39)
	The deviation between the predicted value and the true value is calculated and is not affected by the number of samples.
Goodness of Fit	$\mathrm{R}^2 = \frac{\mathrm{SSE}}{\mathrm{SST}} = 1 - \frac{\mathrm{SSR}}{\mathrm{SST}} = \frac{\sum_{i=1}^{q}(y_j^{\mathrm{out}} - \overline{y})^2}{\sum_{i=1}^{q}(y_j - \overline{y})^2}$ (40)
	When the value of goodness of fit R^2 is greater than 0.8, it shows that the regression line is better to fit the predicted value of the instantaneous incremental wear of the flank.

Table 5. Test set errors.

Mean Square Error MSE	Mean Absolute Error MAE	Root Mean Square Error RMSE	Goodness of Fit R^2
4.02×10^{-16}	1.06×10^{-8}	2.00×10^{-8}	0.82659

According to Table 5, the predicted values of the BPNN prediction model can better reflect the measured values, and the predicted results of the model are accurate. The generalization is excellent, and the instantaneous incremental wear of the flank face of the cutter tooth can be predicted.

When compared to the existing methods for predicting tool wear based on given cutting conditions over a period of time, the proposed method based on BPNN learning has significant advantages in the efficiency and accuracy of predicting the instantaneous incremental wear of the cutter tooth under different instantaneous contact stiffness conditions. When the BP neural network learning model is successfully trained, the model can easily adapt to new cutting conditions. Under new cutting conditions, the number of samples required is very small, or even only a single sample is required. Extract and select special signal features that are relatively more sensitive to the instantaneous wear increment of the cutting surface after the cutter teeth and less sensitive to cutting conditions as inputs to the

meta learning model. The experiments carried out in this study prove that, when compared to the existing neural network learning method reported by previous researchers, using the instantaneous contact stiffness of the cutter tooth flank to predict the instantaneous incremental wear of a specific position has better pertinence and accuracy.

7. Conclusions

1. A method for calculating the instantaneous contact stiffness of the flank face of a cutter tool was proposed, and the distribution characteristics of the instantaneous contact stiffness of the flank under different contact angles and different periods were revealed. The results showed that the distribution of instantaneous contact stiffness over different periods was similar. In the same cutting cycle, the contact stiffness was mainly concentrated in the middle of the cutting edge. With an increase in cutter tooth rotation angle, the contact stiffness increased first and then decreased;
2. The distribution results for incremental wear and cumulative wear depth on the flank showed that the distribution of incremental wear was mainly concentrated near the cutting edge. With an increase in milling cutter rotation angle, the wear area increased first and then decreased, and the value of instantaneous incremental wear also increased first and then decreased. The distribution of contact stiffness and incremental wear on the flank had similar variation characteristics with time;
3. A positioning prediction model for tool flank wear based on the instantaneous contact stiffness of a tool flank was proposed. Four statistical indexes, mean square error, mean absolute error, root mean square error, and goodness of fit, were used as the evaluation criteria for a BP neural network to predict the accuracy of the tool flank wear model. The results showed that the deviation between the predicted value and the measured value for the amount of instantaneous wear at the test point in the prediction model was within 1×10^{-8} mm, which proved that the instantaneous incremental wear of the test point was basically consistent with the actual incremental wear, indicating that the model's prediction result was accurate and the generalization was excellent.

Author Contributions: P.Z.: Conceptualization, Writing—review and editing, Supervision, Project administration, Funding acquisition, Formal analysis. Y.S.: Methodology, Writing—original, Software, Validation, Investigation, Data curation, Draft preparation, Visualization, Formal analysis. B.J.: Conceptualization, Supervision, Project administration, Funding acquisition. B.W.: Software, Investigation, Data curation. All authors have read and agreed to the published version of the manuscript.

Funding: This research was funded by the Natural Science Foundation of China (52105440), and the Nature Science Foundation of Heilongjiang Province of China, ZD2020E008.

Institutional Review Board Statement: Not applicable.

Informed Consent Statement: Not applicable.

Conflicts of Interest: The authors declare no conflict of interest.

References

1. Jiang, B.; Li, W.; Zhao, P.; Fan, L.; Sun, M. Identification of Friction Behavior Variation in the Minor Flank of Square Shoulder Milling Cutters under Vibration. *Appl. Sci.* **2022**, *12*, 4038. [CrossRef]
2. Zhao, P.; Zhang, L.; Jiang, B.; Wang, Y. Instantaneous Friction Energy Consumption and Its Evolution of High Energy Efficiency Milling Cutter. *Adv. Mech. Eng.* **2022**, *14*, 1–18. [CrossRef]
3. Jiang, B.; Xu, X.; Zhao, P.; Fan, L.; Gu, Y. Multi-scale Method for Recognizing Damage in High-efficiency Milling Cutter. *Int. J. Advanced Manuf. Technol.* **2020**, *107*, 2547–2562. [CrossRef]
4. Luo, M.; Luo, H.; Zhang, D.; Tang, K. Improving tool life in multi-axis milling of Ni-based superalloy with ball-end cutter based on the active cutting edge shift strategy. *J. Mater. Process. Technol.* **2018**, *252*, 105–115. [CrossRef]
5. Sugihara, T.; Kobayashi, R.; Enomoto, T. Direct Observations of Tribological Behavior in Cutting with Textured Cutting Tools. *Int. J. Mach. Tools Manuf.* **2021**, *168*, 103726. [CrossRef]

6. Malakizadi, A.; Hajali, T.; Schulz, F.; Cedergren, S.; Ålgårdh, J.; M'Saoubi, R.; Hryha, E.; Krajnik, P. The Role of Microstructural Characteristics of Additively Manufactured Alloy 718 on Tool Wear in Machining. *Int. J. Mach. Tools Manuf.* **2021**, *171*, 103814. [CrossRef]
7. Kong, D.; Chen, Y.; Li, N.; Duan, C.; Lu, L.; Chen, D. Relevance Vector Machine for Tool Wear Prediction. *Mech. Syst. Signal Process.* **2019**, *127*, 573–594. [CrossRef]
8. Sarıkaya, M.; Gupta, M.K.; Tomaz, I.; Pimenov, D.Y.; Kuntoğlu, M.; Khanna, N.; Yıldırım, Ç.V. A State-of-the-art Review on Tool Wear and Surface Integrity Characteristics in Machining of Superalloys. *CIRP J. Manuf. Sci. Technol.* **2021**, *35*, 624–658. [CrossRef]
9. Yang, W.A.; Zhou, Q.; Tsui, K.L. Differential Evolution-based Feature Selection and Parameter Optimisation for Extreme Learning Machine in Tool Wear Estimation. *Int. J. Prod. Res.* **2016**, *54*, 4703–4721. [CrossRef]
10. Zhu, K.; Zhang, Y. A Generic Tool Wear Model and Its Application to Force Modeling and Wear Monitoring in High Speed Milling. *Mech. Syst. Signal Process.* **2019**, *115*, 147–161. [CrossRef]
11. Taylor, F.W. *On the Art of Cutting Metals*; American Society of Mechanical Engineers: New York, NY, USA, 1906.
12. Sick, B. On-line and Indirect Tool Wear Monitoring in turning with Artificial Neural Networks: A Review of More than a Decade of Research. *Mech. Syst. Signal Process.* **2002**, *16*, 487–546. [CrossRef]
13. Ni, C.; Zhu, L.; Yang, Z. Comparative Investigation of Tool Wear Mechanism and Corresponding Machined Surface Characterization in Feed-direction Ultrasonic Vibration Assisted Milling of Ti–6Al–4V from Dynamic View. *Wear* **2019**, *436*, 203006. [CrossRef]
14. Mao, C.; Zhang, Y.; Peng, X.; Zhang, B.; Hu, Y.; Bi, Z. Wear Mechanism of Single cBN-WC-10Co Fiber Cutter in Machining of Ti-6Al-4V Alloy. *J. Mater. Process. Technol.* **2018**, *259*, 45–57. [CrossRef]
15. Bouzakis, K.D.; Michailidis, N.; Vidakis, N.; Efstathiou, K. Failure Mechanisms of Physically Vapour Deposited Coated Hardmetal Cutting Inserts in Turning. *Wear* **2001**, *248*, 29–37. [CrossRef]
16. Rehorn, A.; Jiang, J.; Orban, P. State-of-the-art Methods and Results in Tool Condition Monitoring: A Review. *Int. J. Adv. Manuf. Technol.* **2005**, *26*, 693–710. [CrossRef]
17. Cai, T.L.; Ma, Y.; Huang, C.; Yao, X. Swept Area Modeling and Cutter Wear study in Turn-milling. *Int. J. Adv. Manuf. Technol.* **2015**, *80*, 775–789.
18. Oliveira, A.J.; Diniz, A.E. Tool Life and Tool Wear in the Semi-finish Milling of Inclined Surfaces. *J. Mater. Process. Technol.* **2009**, *209*, 5448–5455. [CrossRef]
19. Liao, J.; Zhang, J.; Feng, P.; Yu, D.; Wu, Z. Identification of Contact Stiffness of Shrink-fit tool-Holder Joint Based on Fractal Theory. *Int. J. Adv. Manuf. Technol.* **2017**, *90*, 2173–2184. [CrossRef]
20. Feng, J.; Wan, M.; Dong, Z.-Y.; Zhang, W.-H. A Unified Process Damping Model Considering the Varying Stiffness of the Milling System. *Int. J. Mach. Tools Manuf.* **2019**, *147*, 103470. [CrossRef]
21. Morelli, L.; Grossi, N.; Campatelli, G.; Scippa, A. Surface Location Error Prediction in 2.5-axis Peripheral Milling Considering Tool Dynamic Stiffness Variation. *Precis. Eng.* **2022**, *76*, 95–109. [CrossRef]
22. Nguyen, H.T.; Wang, H.; Hu, S.J. Modeling Cutter Tilt and Cutter-spindle Stiffness for Machine Condition Monitoring in Face Milling Using High-definition Surface Metrology. *Int. J. Adv. Manuf. Technol.* **2014**, *70*, 1323–1335. [CrossRef]
23. Liu, S.; Jin, Q.; Wang, P. Effect of Additional Supports on Surface Errors in the Peripheral Milling of a Flexible Workpiece. *Int. J. Mater. Prod. Technol.* **2008**, *31*, 214–223. [CrossRef]
24. Schmitz, T.L.; Powell, K.; Won, D.; Duncan, G.S.; Sawyer, W.G.; Ziegert, J.C. Shrink Fit Tool Holder Connection Stiffness/Damping Modeling for Frequency Response Prediction in Milling. *Int. J. Mach. Tools Manuf.* **2007**, *47*, 1368–1380. [CrossRef]
25. Liu, J.; Ma, C.; Wang, S.; Wang, S.; Yang, B. Contact Stiffness of Spindle-tool Holder Based on Fractal Theory and Multi-scale Contact Mechanics Model. *Mech. Syst. Signal Process.* **2019**, *119*, 363–379. [CrossRef]
26. You, Z.; Gao, H.; Guo, L.; Liu, Y.; Li, J.; Li, C. Machine Vision Based Adaptive Online Condition Monitoring for Milling Cutter under Spindle Rotation. *Mech. Syst. Signal Process.* **2022**, *171*, 108904. [CrossRef]
27. Zhang, X.; Gao, Y.; Guo, Z.; Zhang, W.; Yin, J.; Zhao, W. Physical Model-based Tool Wear and Breakage Monitoring in Milling Process. *Mech. Syst. Signal Process.* **2023**, *184*, 109641. [CrossRef]
28. Nouri, M.; Fussell, B.K.; Ziniti, B.L.; Linder, E. Real-time Tool Wear Monitoring in Milling Using a Cutting Condition Independent Method. *Int. J. Mach. Tools Manuf.* **2015**, *89*, 1–13. [CrossRef]
29. Song, G.; Zhang, J.; Zhu, K.; Ge, Y.; Yu, L.; Fu, Z. Tool Wear Monitoring Based on Multi-kernel Gaussian Process Regression and Stacked Multilayer Denoising AutoEncoders. *Mech. Syst. Signal Process.* **2023**, *186*, 109851. [CrossRef]
30. Lavella, M.; Botto, D. Fretting Wear Characterization by Point Contact of Nickel Superalloy Interfaces. *Wear* **2011**, *271*, 1543–1551. [CrossRef]
31. Zhupanska, O.I. Contact problem for Elastic Spheres: Applicability of the Hertz Theory to Non-small Contact Areas. *Int. J. Eng. Sci.* **2011**, *49*, 576–588. [CrossRef]
32. Butt, H.J.; Pham, J.T.; Kappl, M. Forces between a stiff and a soft surface. *Curr. Opin. Colloid Interface Sci.* **2017**, *27*, 82–90. [CrossRef]
33. Usui, E.; Shirakashi, T.; Kitagawa, T. Analytical Prediction of Cutting Tool Wear. *Wear* **1984**, *100*, 129–151. [CrossRef]
34. Jiang, B.; Xu, T.; Li, Z.; Gu, Y.P.; He, T.T. Characterisation for differential wear between left and right flank faces in turning large pitch internal thread. *Int. J. Mechatron. Manuf. Syst.* **2018**, *11*, 325–347. [CrossRef]

35. Wei, Y.; Zhao, Y.; Lu, C.; Wei, S.; Liu, L.; Zhu, Z.; Yan, S. Cross-modal Retrieval with CNN Visual Features: A New Baseline. *IEEE Trans. Cybern.* **2016**, *47*, 449–460. [CrossRef] [PubMed]
36. Karim, F.; Majumdar, S.; Darabi, H.; Harford, S. Multivariate LSTM-FCNs for Time Series Classification. *Neural Netw.* **2019**, *116*, 237–245. [CrossRef] [PubMed]
37. Goodfellow, I.; Pouget-Abadie, J.; Mirza, M.; Xu, B.; Warde-Farley, D.; Ozair, S.; Courville, A.; Bengio, Y. Generative Adversarial Networks. *Commun. ACM* **2020**, *63*, 139–144. [CrossRef]
38. Zhang, H.; Wang, Z.; Liu, D. A Comprehensive Review of Stability Analysis of Continuous-time Recurrent Neural Networks. *IEEE Trans. Neural Netw. Learn. Syst.* **2014**, *25*, 1229–1262. [CrossRef]
39. He, F.; Zhou, J.; Feng, Z.-K.; Liu, G.; Yang, Y. A Hybrid Short-term Load Forecasting Model Based on Variational Mode Decomposition and Long Short-term Memory Networks Considering Relevant Factors with Bayesian Optimization Algorithm. *Appl. Energy* **2019**, *237*, 103–116. [CrossRef]
40. Meng, X.; Zhang, J.; Xiao, G.; Chen, Z.; Yi, M.; Xu, C. Tool Wear Prediction in Milling Based on a GSA-BP Model with a Multisensor Fusion Method. *Int. J. Adv. Manuf. Technol.* **2021**, *114*, 3793–3802. [CrossRef]
41. Wei, W.; Cong, R.; Li, Y.; Abraham, A.D.; Yang, C.; Chen, Z. Prediction of tool wear based on GA-BP neural network. *Proc. Inst. Mech. Eng. Part B-J. Eng. Manuf.* **2022**, *236*, 1564–1573. [CrossRef]

Disclaimer/Publisher's Note: The statements, opinions and data contained in all publications are solely those of the individual author(s) and contributor(s) and not of MDPI and/or the editor(s). MDPI and/or the editor(s) disclaim responsibility for any injury to people or property resulting from any ideas, methods, instructions or products referred to in the content.